metals

Article

Analysis of the Main Aspects Affecting Bonding in Stainless Steel Rebars Embedded in a Hydraulic Medium

Fernando Ancio [1], Esperanza Rodriguez-Mayorga [2,*] and Beatriz Hortigon [1]

[1] Departamento de Mecánica de Medios Continuos y Teoría de Estructuras, Escuela Politécnica Superior, Universidad de Sevilla, 41011 Seville, Spain; ancio@us.es (F.A.); bhortigon@us.es (B.H.)
[2] Departamento de Estructuras de Edificación e Ingeniería del Terreno, Escuela Técnica Superior de Arquitectura, Universidad de Sevilla, 41012 Seville, Spain
* Correspondence: espe@us.es; Tel.: +34-954-556-602

Abstract: The use of stainless steel rebars to reinforce masonry structures has become established as an eminently efficient methodology. From among the numerous techniques available, bed-joint structural repointing and superficial reinforcement with rebars or meshes attached to surfaces have become widespread, thanks to the excellent results they have produced in recent decades. Both techniques imply the use of diameters less than 6 mm and thin coverings. This article deals with the characterization of the bonding behavior of the rebar under these special circumstances. To this end, several finite element analyses have been carried out to identify the possible relationships between pull-out forces in various situations. These models allow certain conclusions to be drawn regarding the influence of the thickness of covering, boundary conditions, and geometrical aspects of the rebars in bonding. Certain mathematical expressions that relate the various conclusions from this research are finally laid out.

Keywords: masonry reinforcement; stainless rebar; finite element analysis; bonding behavior; boundary conditions

check for updates

Citation: Ancio, F.; Rodriguez-Mayorga, E.; Hortigon, B. Analysis of the Main Aspects Affecting Bonding in Stainless Steel Rebars Embedded in a Hydraulic Medium. *Metals* **2021**, *11*, 786. https://doi.org/10.3390/met11050786

Academic Editor: Fernando Castro

Received: 24 March 2021
Accepted: 10 May 2021
Published: 12 May 2021

Publisher's Note: MDPI stays neutral with regard to jurisdictional claims in published maps and institutional affiliations.

Copyright: © 2021 by the authors. Licensee MDPI, Basel, Switzerland. This article is an open access article distributed under the terms and conditions of the Creative Commons Attribution (CC BY) license (https://creativecommons.org/licenses/by/4.0/).

1. Introduction

The repair of masonry structures concerns society. Historical towns not only form part of the historical and cultural heritage but also constitute a major source of income for the economy of many countries worldwide. Historical towns are usually composed of mainly humble dwellings with a few impressive and magnificent buildings, such as cathedrals and palaces. The origin of all these buildings commonly dates back to the XVIIIth century or even earlier. This fact leads to the conclusion that the constructive system in most of these buildings is that of masonry. On the other hand, the suburbs generally accommodate the majority of the population in large cities, a number of which are ancient neighborhoods without any historical or artistic value, but have also been built with masonry. In this last case, the repair of masonry becomes a social problem for administrations since the repair must be carried out on a reduced budget while preventing the reallocation of residents as far as possible. The development of repair and consolidation techniques for all types of masonry has therefore awakened the interest of many administrations.

Historical masonry is usually composed of three layers: two external layers of stone units infilled with rubble masonry, all pointed with poor lime mortar. In more recent masonries, brick pieces are commonly joined with cement mortars. Many of the repair and consolidation techniques usually applied to masonry structures include the introduction of connectors and/or reinforcements. These have traditionally been steel pieces located either in parallel or perpendicular to the wall faces [1,2]. This reinforcement is frequently introduced into the bed-joints, thereby preventing damage to the masonry units [3–5]. This repair and consolidation methodology, particularly known as bed-joint structural repointing, is especially suitable for historic masonries since it almost totally respects the original materials that compose the structural elements. This technique is currently applied by substituting the steel rebars with fibers, thus attaining a more respectful way to repair walls since smaller sections of reinforcements are required than when steel pieces are used [6]. The main disadvantage of this technique is, obviously, its cost. The cost of this technique makes it unaffordable in many cases, not only due to the cost of the fibers but also to the execution of the work itself. The use of steel rebars instead of fiber plates contributes significantly towards reducing the cost of the application of the technique. Even if stainless steel is chosen, the cost can be reduced by approximately 500% when compared with fibers. The use of stainless steel is almost compulsory when repairing historical masonries since traditional dwellings are usually affected by rising damp [7]. Furthermore, if masonry without any historical or artistic value is being repaired, then there is no issue with introducing the reinforcement into drills and grooves or placing them superficially inside renders.

These reinforcements, whose effectiveness is widely demonstrated, constitute one of the most financially feasible techniques of repair and consolidation available today. Steel rebars with diameters up to 6 mm normally provide the reinforcements. A particular feature shared by these reinforcements is the mortar thicknesses that cover the rebars, which are usually thinner than those existing in reinforced concrete. The reason is obviously linked to the small cavity in which the rebar is usually introduced, as well as the thin layer of mortar that embeds the rebars when they are superficially placed [8,9]. This fact has traditionally been disregarded, however, since there are no special standardized tests to determine the bonding behavior of rebars placed as described. Furthermore, the fact that only bars with small diameters are used in these repairs also modifies their bonding behavior since no linear relationship has been identified between the diameter and load transfer of bars [10]. Lastly, the shape of the bars exerts a strong influence on bonding, but this is poorly documented regarding bars with diameters of up to 10 mm embedded in a medium different from concrete [11,12].

The beam test, as the standard bonding test collected in codes [13] aims to determine the force needed to extract a rebar with diameter of up to 16 mm from a prism of concrete that has effective coverings of 50 mm in three of the faces. The lack of codes for the particular situation of bars reinforcing masonries leads to the necessity for the adaptation of them from similar fields. The bonding of anchors can be regulated by the British Standard BS EN 1881:2006 [14], while BS EN 846-2:2001 [15] can be applicable to bed-joint structural repointing. The codes establish the measurement of the axial force to pull out the rebar from 30-mm grouted drills or from its position in the brick joint, respectively. On the other hand, RILEM-TC RC6 [16] opens the door to a simpler test from the point of view of the development of the samples. The aim of this test is to determine the pull-out force necessary to pull out a bar embedded in a cube whose edge measures 10 times the diameter of the bar and is fixed in the face in which the bar is inserted. A similar test is proposed for fibers when used to reinforce masonry structures [17]. The variety of codes available drives undoubtedly to the fact that results from various studies are incomparable, since they depend on the criteria followed when obtained [18–20].

The bonding of bars to reinforce masonry is barely documented. The aim of this paper is to research the influence that the different requirements of codes have on the final bond behavior of the bar. Since this research is oriented towards the reinforcement of masonry, stainless steel rebars embedded in prisms of hydraulic materials are analyzed under a variety conditions: (i) effective covering; (ii) boundary conditions; (iii) Young's modulus value of covering; and (iv) ribs of bar geometry.

The finite element (FE) method has been chosen for the analysis of the bonding behavior in the aforementioned specific circumstances. In this research, a complete 3D analysis of the ribbed bars was carried out in order to attain a more precise reproduction of the behavior of the rebars in terms of bonding than those achieved using macro models [21,22]. Finally, several conclusions are drawn regarding the influence of these different parameters on bonding.

2. Materials and Methods

Rebars were modelled by means of the software CAD Rhinoceros 3D. This software, together with its plug-in Grasshopper 3D, eases the parameterization and model generation for their later finite element analysis. In all cases, rebars with 30 mm length and 5 mm diameter have been analyzed. The bar shape adopted for these analyses is based on the standard stainless-steel bar, of which the transverse section is composed of the filleted intersection of three arcs (Figures 1 and 2a).

Figure 1. Standard stainless-steel rebar.

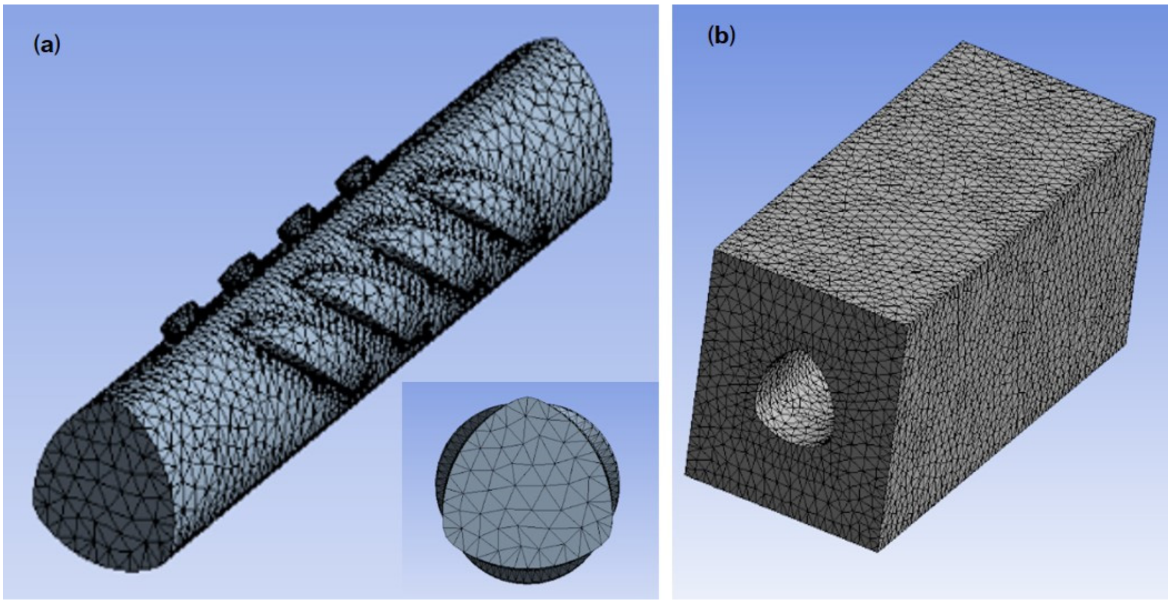

Figure 2. Finite element model for the rebar embedded in a prism of mortar whose base measures 12 mm × 12 mm: (**a**) model of the rebar; (**b**) model of the prism of mortar that surrounds the rebar.

Altogether, 280 3D solid finite element analyses have been carried out by means of the software ANSYS R19.3 for the development of this research. All the models consist of a rebar embedded in a prism of hydraulic material, reproducing the media in which rebar are inserted. Since rebars are usually surrounded by mortar or grout made with hydraulic binders (mainly lime, cement or mixtures of both), the properties assigned to the prisms are those of a generic repairing mortar. The contact between rebars and the mortar joints was defined through a cohesive model zone. In all these samples, geometrical and mechanical parameters were changed iteratively, measuring, this way, the influence of each of them in the final results in terms of bonding. Thus, (i) 16 samples were analyzed in order to calibrate the influence of the resistant properties in the cohesive model zone; (ii) in 96 samples, effective covering values ranging from 6 to 25 mm were combined with four different values of Young's modulus of the mortar joints that embedded the bars and four different boundary conditions; and finally, (iii) 168 analyses were carried out based on 42 different rib shapes, which were analyzed effectively, covered with 6 and 25 mm, as well as under two different boundary conditions.

In all the analyses, the failure of masonry by pull-out forces has been dismissed since it falls outside the scope of this research. The failure of the samples can be therefore deduced as being due to (i) excessive tensile stresses in reinforcements, which is highly improbable; (ii) cone failure of the mortar embedment, which occurs when a small part of the covering around the bar fails; (iii) sliding of the set rebar–medium along the interface between the masonry and the mortar; and (iv) sliding along the steel–mortar interface. Failure mode (ii) is taken into account when modelling the mortar joints through the microplane model by finite element analysis (Section 2.2). Regarding sliding failures, this research only considers (iv), since (iii) is considered negligible in comparison with (iv), especially regarding rebars with thin coverings [10,23]. Figure 2 depicts one of the finite element samples. As a final result, the number of nodes and elements of models ranges from 22,159 nodes to 29,223 nodes, and 98,010 elements to 124,890 elements. The descriptions of the numerical models of both the failure modes considered are addressed in the following subsections.

2.1. Modelling Rebars by Finite Elements

When rebars are employed to reinforce masonry structural elements, they are always expected to be generously less than the proportional limit of steel. For this reason, steel has been defined as an isotropic elastic linear material with E = 210 GPa and Poisson modulus $\nu = 0.3$. Elements type 3D Solid have been employed to model the rebars and the mortar joints that surrounds them. Specifically, a tetrahedral 8-node solid element with three degrees of freedom at each node, i.e., Solid 185, was used [24]. This element has properties such as plasticity, stress-stiffening, large deflection, and large strain capabilities, which make it suitable for modelling rebars (Figure 2a).

2.2. Modelling Mortar Joints by Finite Elements

Mortars present non-linear behavior as well as differences in their responses under tensile and compressive stresses. Regarding tensile strength (f_t), sudden softening occurs accompanied by a reduction in stiffness. On the other hand, in compressive strength (f_c), stress–strain behavior will first involve ductile hardening followed by softening and reduction in the stiffness. This behavior, defined as quasi-brittle, cannot be represented by the slip theory of plasticity, since the inelastic behavior in the microscale does not physically represent a slip. The microplane model is suitable for quasi-brittle materials, since it has provided good results in similar previous experiences [12,25].

The microplane model was first enunciated by Taylor [26,27] and later developed and settled by the authors [28–33]. Microplane theory discretizes materials into 42 symmetrically located planes that define a 42-faced polyhedron (tetracontadihedron). By applying a simple constitutive law to each plane, the theory extrapolates the initial plane model to a consistent three-dimensional model. Microplane theory analyzes the physical phenomena occurring in the microstructure of the material by analyzing the physical phenomena occurring on each plane, thus reproducing the anisotropic damage.

The microplane model establishes for each of the 42 microplanes the value of equivalent strain energy (η^{mic}) as obtained by [34]:

$$\eta^{mic} = k_0 I_1 + \sqrt{k_1^2 I_1^2 + k_2 J_2} \tag{1}$$

where I_1 and J_2 are the first invariant of the strain tensor and the second invariant of the deviatoric part of the strain tensor ε, respectively:

$$I_1 = \varepsilon_1 + \varepsilon_2 + \varepsilon_3 \tag{2}$$

$$J_2 = \frac{1}{6}\left[(\varepsilon_1 + \varepsilon_2)^2 + (\varepsilon_2 + \varepsilon_3)^2 + (\varepsilon_1 + \varepsilon_3)^2\right] \tag{3}$$

and k_0, k_1, and k_2 are constants whose values are set as follows [35–37]:

$$k_0 = k_1 = (k-1)/(2k(1-2v)) \tag{4}$$

$$k_2 = 3/\left(k(1+v)^2\right) \tag{5}$$

where υ is Poisson's ratio and k is the ratio between the compressive and tensile strength of the material $k = f_c/f_t$.

When the material is working under its proportional limit, the strain tensor ε can be easily obtained through Young's modulus and Poison's ratio. This elastic behavior ceases when in any of the 42 microplanes η^{mic} reaches a certain value γ_0^{mic}. Then, the material damage is considered to be initiated, and the material response is affected by the damage parameter d^{mic}:

$$d^{mic} = 1 - \frac{\gamma_0^{mic}}{\eta^{mic}}\left[1 - \alpha^{mic} + \alpha^{mic} \cdot exp\left(\beta^{mic}\left(\gamma_0^{mic} - \eta^{mic}\right)\right)\right] \tag{6}$$

where α^{mic} is the maximum degradation coefficient; β^{mic} is the rate of damage evolution (shape of the softening curve), and γ_0^{mic} is the equivalent strain energy when the material damage starts. When the damage starts, the material response is reduced by the factor $(1 - d^{mic})$, with d^{mic} ranging from 0 to 1, where 0 is an undamaged material and 1 a totally damaged material where the stiffness is lost.

The microplane model with damage is implemented in ANSYS R19.3 through the element Solid 185, described in Section 2.1. The microplane model in ANSYS R19.3 is defined through Young's modulus and Poisson's ratio as well as via the six constants C_1, C_2, C_3, C_4, C_5, and C_6. The values of these constants were set as k_0, k_1, k_2, γ_0^{mic}, α^{mic}, and β^{mic}, respectively. In this research, in accordance with the mechanical properties of a hydraulic mortar, previous experiences [34,38] and by comparison with results obtained from laboratory tests [39], the C constants were set to 0.729, 0.729, 0. 26, 6×10^{-5}, 0.75, and 100. These values provide quality results since the behavior of the sample predicted by finite element analysis is compatible with that published in literature for mortars specially designed to be used in repairing and retrofitting tasks (Figure 3). Young's modulus iteratively takes the values 5.6, 10, 20, and 50 GPa, thereby considering several possibilities of hydraulic mortars usually employed in repairing masonries, from poor-quality lime mortars to the high-performance grouts based on micro fine hydraulic binders. Poisson's ratio was set to 0.2 [40–44].

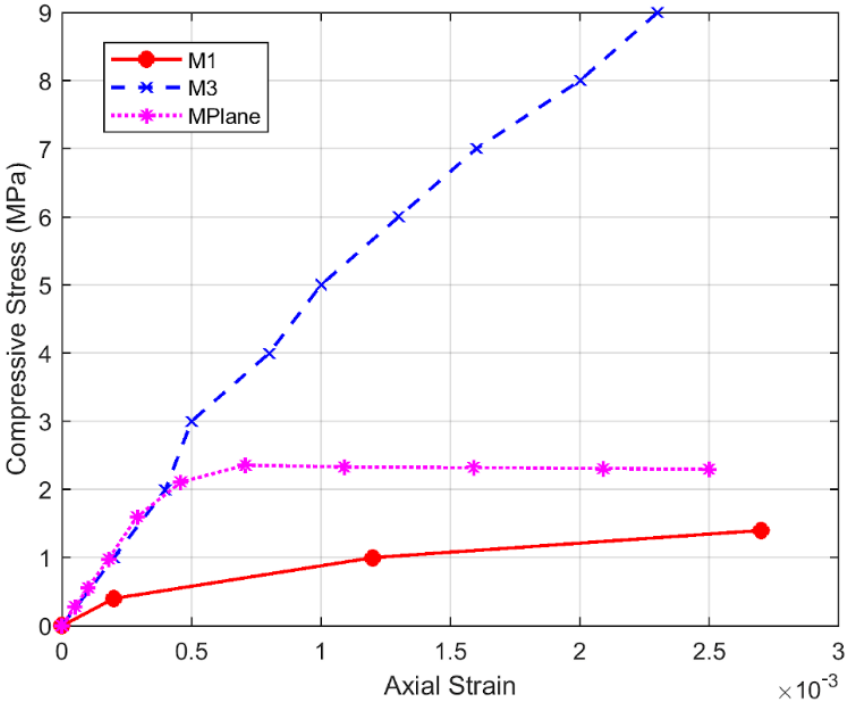

Figure 3. Comparison of the stress-strain behavior of samples of hydraulic mortars obtained in the laboratory (M1 and M3) from literature [39] and analyzed by finite elements for this research (MPlane).

2.3. Modelling Contacts

The correct reproduction of the bonding behavior of the samples by the FE models depends on the definition of contact parameters. Three phenomena occur in the interface [45–48]: (i) friction, due to the joint action of dilation slip and shear failure of the grout; (ii) mechanical interlock, mainly dependent on rib shape and rib separation; and (iii) chemical adhesion between the rebar and the media in which it is inserted. The cohesive zone model with mixed debonding interface (henceforth, CZM) reflects the behavior of the conjunct in terms of points (i) and (ii), since (iii) is usually disregarded due to its low influence in bonding [46]. CZM is modelled through elements CONTA174 and TARGE170. Elements type CONTA are used to represent contact and sliding between surfaces. The contact is pair based, with the target surface defined by the 3D target element type [24].

A CZM is defined though maximum values of bonding stress that, when exceeded, lead to the failure of the contact by slippage and/or separation between surfaces. This failure can be due to normal stress or shear stress, both being limited by the values of the maximum bond tensile stress and maximum bond shear stress. Many studies use macro models or simplified axisymmetric models for ribbed bars [21,49,50]. These works involve modeling plain bars where bond tensile stress does not influence the final results, and fictitious values of bond shear stress supply the absence of the rib. Since this research involves the consideration of real rib shapes to evaluate their influence on bonding, a sensitivity analysis was previously carried out to calibrate the values for maximum bond shear stress and maximum bond tensile stress given to the CZM. This analysis consisted of the finite element analysis of a rebar embedded in a cube with 100 mm edge, simulating a pull-out test. A longitudinal displacement of 5×10^{-5} mm was imposed on the rebar while the face of the cube in which the rebar was inserted was maintained as fixed. In this study, maximum bond shear and bond tensile stresses were fixed at 0.10, 0.25, 0.50, and 1.00 MPa. The results were analyzed in terms of the reaction force (F) transferred from the rebar to the cube of the mortar. The results are depicted in Figure 4 and can be found in greater detail in Appendix A.

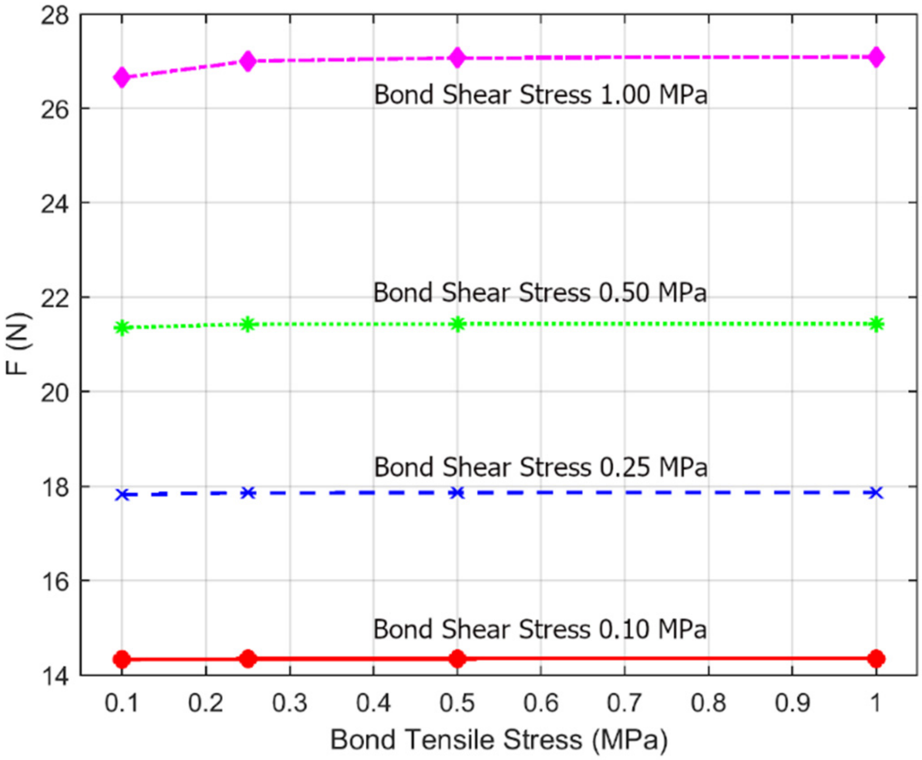

Figure 4. Values of the reaction force transferred from the bar to the surrounding media (100-mm-edge cube) for a displacement equal to 5×10^{-5} mm.

These 16 calculations confirm that maximum bond tensile stress has effects on the bonding behavior of the rebar. This thesis was previously enunciated for plain bars [23]. It is hereby confirmed that changing the limit of the bond tensile stress, which appears only in one of the rib faces, fails to significantly modify the bonding behavior of rebars. Thus, bonding behavior depends on the value of the maximum bond shear stress that is set, as well as on the compression strength of the mortar joints opposed to the compressed face of the ribs. When high values of bond shear stress are set, a homogeneous distribution of frictional stresses is obtained: this distribution is obviously unfeasible. In contrast, setting the maximum bond shear stress at lower values involves a stress distribution that is perfectly feasible (Figure 5). Therefore, maximum values were set to 0.10 MPa for bond shear stress and 1 MPa for bond tensile stress.

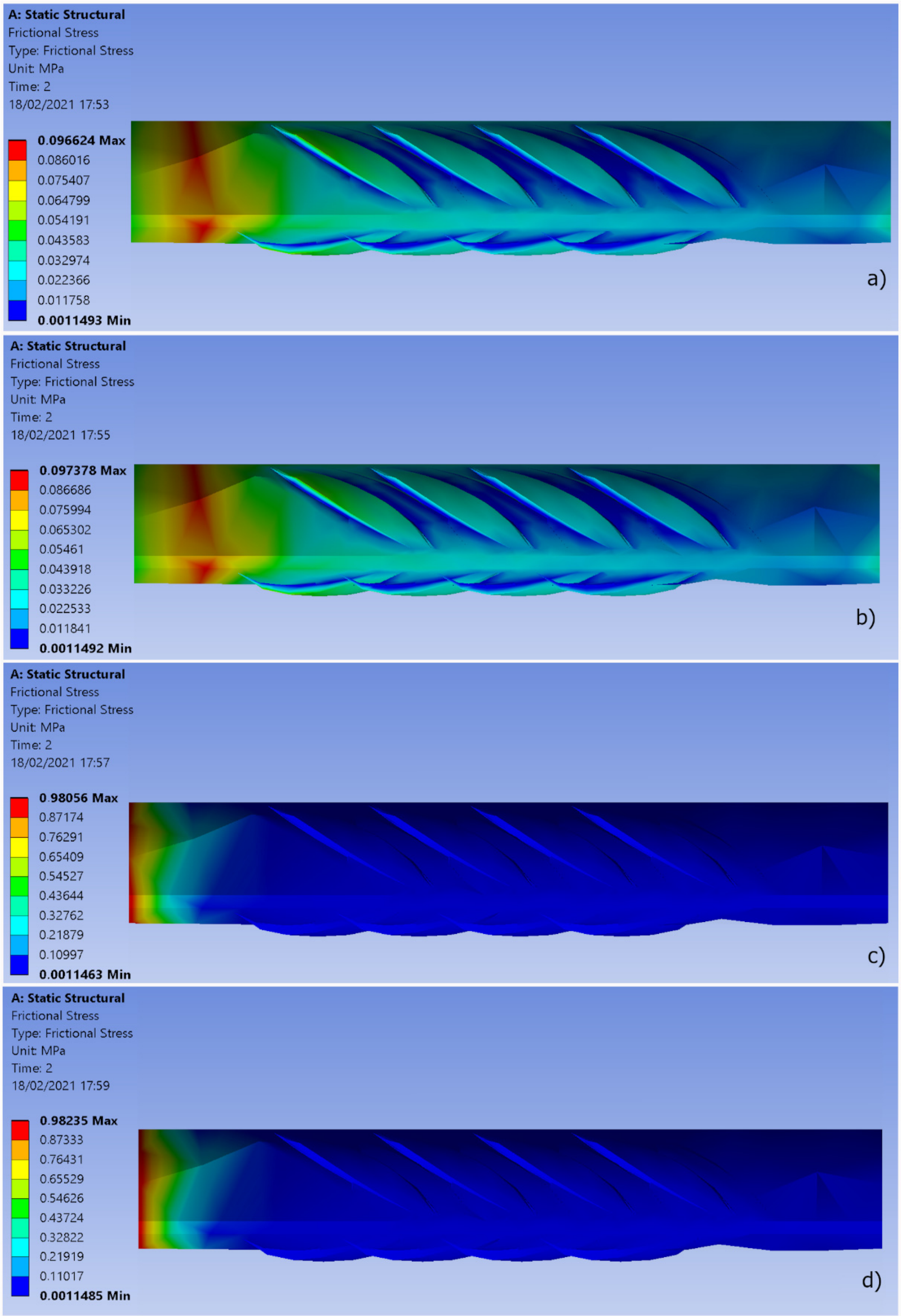

Figure 5. Bond shear stress (MPa) measured at the rebar–mortar interface for a displacement equal to 5×10^{-5} mm from a 100-mm-edge cube, where maximum bond shear stress and bond tensile stress (both in MPa) were set to (**a**) 0.10/0.10; (**b**) 0.10/1.00; (**c**) 1.00/0.10; (**d**) 1.00/1.00.

3. Results

The results obtained from all the analyses are presented in this section and are subsequently discussed in Section 4. As in the previous sections, the results are presented in terms of the reaction force (F) induced in the medium when the rebar was longitudinally displaced 5×10^{-5} mm from its initial position. Ninety-six samples were analyzed taking into account several values of the thickness of the covering and Young's modulus of the mortar in which the rebar is embedded as well as different boundary conditions (Section 3.1). On the other hand, 42 samples were obtained for different rib shapes and were analyzed under different boundary conditions and with two values of effective covering (Section 3.2).

3.1. Thickness of Covering, Boundary Conditions, and Material

The results of the effect of the thickness of covering, boundary conditions, and Young's modulus of material in which the rebar is embedded are shown in Table 1. In these analyses, different values for the parameters were combined while the fixed values of 30 mm and 5 mm were taken for the rebar length and rebar diameter, respectively.

Table 1. Reaction force F (N) needed to longitudinally displace a rebar 5×10^{-5} mm from a prism of mortar under various geometrical and mechanical conditions.

Boundary Conditions	Effective Covering (mm)	F (N)			
		* E_1	* E_2	* E_3	* E_4
Fixed base (1)	6	4.846	8.07	13.769	26.074
	7.5	6.479	10.779	18.287	34.375
	10	8.636	14.384	24.432	44.732
	12.5	10.251	17.075	28.89	49.997
	15	10.539	17.648	30.021	50.605
	25	12.633	20.941	34.734	49.328
Two fixed lateral faces (2, 3)	6	12.91	22.275	35.564	50.379
	7.5	12.67	21.987	37.243	50.698
	10	10.33	18.066	33.671	50.172
	12.5	8.91	15.637	29.947	50.406
	15	6.82	12.021	23.319	47.906
	25	5.512	9.741	19.029	42.943
Three fixed lateral faces (2, 3, 4)	6	17.899	30.457	43.622	49.251
	7.5	17.358	29.775	44.931	50.366
	10	13.916	24.158	42.513	50.126
	12.5	11.894	20.745	38.599	50.094
	15	9.024	15.834	30.348	48.786
	25	7.446	13.112	25.371	49.535
Four fixed lateral faces (2, 3, 4, 5)	6	20.502	34.492	43.613	50.869
	7.5	19.552	33.238	44.414	51.268
	10	15.441	26.706	44.889	50.568
	12.5	13.089	22.768	41.415	50.317
	15	9.858	17.262	32.917	48.821
	25	8.124	14.287	27.546	48.663

* Values of Young's modulus (GPa): $E_1 = 5.6$, $E_2 = 10$, $E_3 = 20$, $E_4 = 50$.

Regarding the thickness of covering, rebars were embedded in mortar prisms with base A × A, where A was changed iteratively: 12, 15, 20, 25, 30, and 50 mm. This assumes effective coverings of 6, 7.5, 12.5, 15, and 25 mm, respectively, which always remain below the minimum values established by codes, as was presented in Section 1. On the other hand, Young's modulus of hydraulic material that composes prisms surrounding the rebars had values of 5.6, 10, 20, and 50 GPa. Finally, prisms that surround rebars were fixed in their base (face number 1), two lateral faces (face numbers 2 and 3), three lateral faces (face numbers 2, 3, and 4), and four lateral faces (face numbers 2, 3, 4, and 5) iteratively in each analysis (Figure 6).

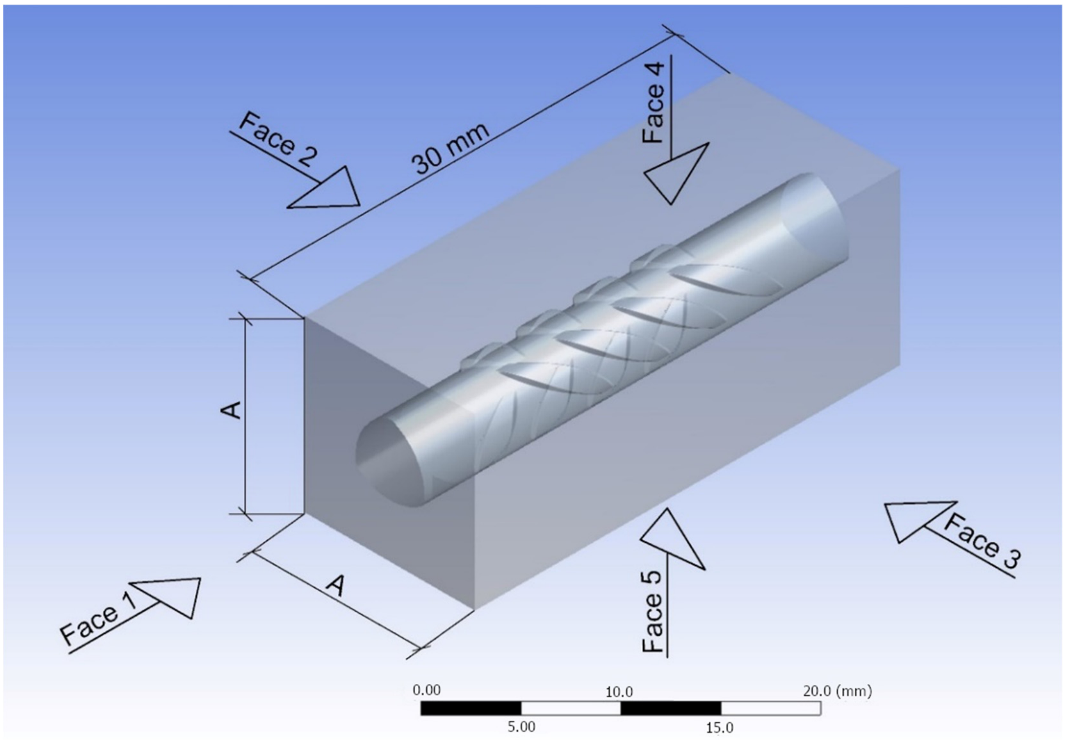

Figure 6. Diagram depicting the parameterization of samples to set the different mechanical and geometrical characteristics of each of the finite element analyses carried out.

To better understand load transference from rebar to mortar joints, as well as the failure mechanisms of rebars with small diameters thinly covered, an analysis of the slippage failure was carried out. This analysis consisted of augmenting the value of the displacement imposed up to failure of the interface. It was carried out twice. In both analyses, mortar with Young's modulus of 5.6 MPa and rebar effectively covered with 7.5 mm were set. These samples were analysed when (i) the base (face number 1) was fixed and when (ii) three lateral faces were fixed (face numbers 2, 3, 4). Figure 7 represents the force transferred to the mortar in the function of the longitudinal displacement of the rebar for every load step-up to failure in cases (i) and (ii). The maximum force in (ii) assumes a 90.2% increment with respect to (i). Stress distribution for (i) for 40%, 60%, and 100% of the force transferred from the rebar to the mortar when failure occurs is presented in Figure 8, while Figure 9 depicts similar load steps for (ii).

Figure 8a–c show bonding shear stress distribution for 40%, 60%, and 100% of the failure load, respectively, when the rebar is embedded in a prism fixed in the base (face number 1). In the first steps of the simulation (Figure 8a), the load is mainly transferred to the area of the rebar close to the application of the displacement. Despite the fact that only 40% of the maximum force was transferred, the maximum value of bonding shear stress (0.1 MPa) was reached in some points. Later in the simulation, the area of the rebar close to the application of the displacement (Figure 8b,c) fails due to slippage and does not transfer any force. Figure 8d–f show bonding normal stresses for 40%, 60%, and 100% of the failure load, respectively. These three pictures show clearly how only the compressed area of the ribs closest to the area where the displacement was applied contributed to the force transference.

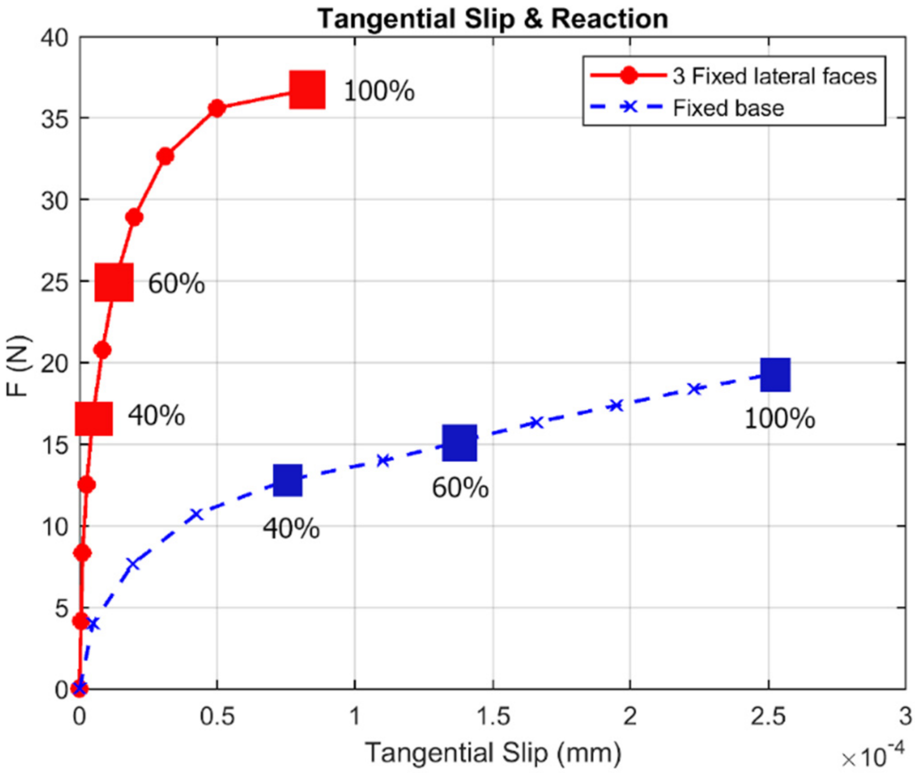

Figure 7. Displacement (mm) vs. force transferred to the mortar joints by rebars embedded in mortar with 5.6 GPa Young's modulus and 7.5 mm of effective covering up to failure under two different boundary conditions.

Figure 9a–c depict bonding shear stress distribution when the rebar transferred 40%, 60%, and 100% of the force transferred in failure, respectively, and the rebar was embedded in a mortar prism fixed in three of the four longitudinal faces (faces number 2, 3, and 4). From the beginning of the simulation, these pictures show that the whole rebar contributes to the load transfer mechanism. Figure 9d–f represent bonding normal stress distribution for the load steps previously described. Although only in the last load steps did the ribs work under compression, it is remarkable that all ribs contributed to the force transference mechanism. As a consequence, compressive values were significantly lower than those attained when only the base face (face number 1) was fixed: 1.6459 MPa (Figure 8f) compared to 0.61233 MPa (Figure 9f).

3.2. *Rib Shape*

Rib shape is one of the key values regarding bonding in rebars. Various rebar shapes were analyzed in order to check their performance in terms of bonding behavior. Rebar geometry was parameterized as depicted in Figure 10, and the values of the parameters ranged as follows between those recommended in the codes [51–53]: (i) central width, *Wc*, from 1.0 to 3.5 mm; (ii) extreme width, *We*, from 1.0 to 3.5 mm; (iii) angle between the rib and rebar axes, *B*, from 35° to 75°; (iv) rib-face angles, *Bf*, from 45° to 90°; (v) rib height in the central transversal section of the rib, *hr*, from 0.15 to 0.75 mm; (vi) rib spacing; *s*, from 3 to 6 mm.

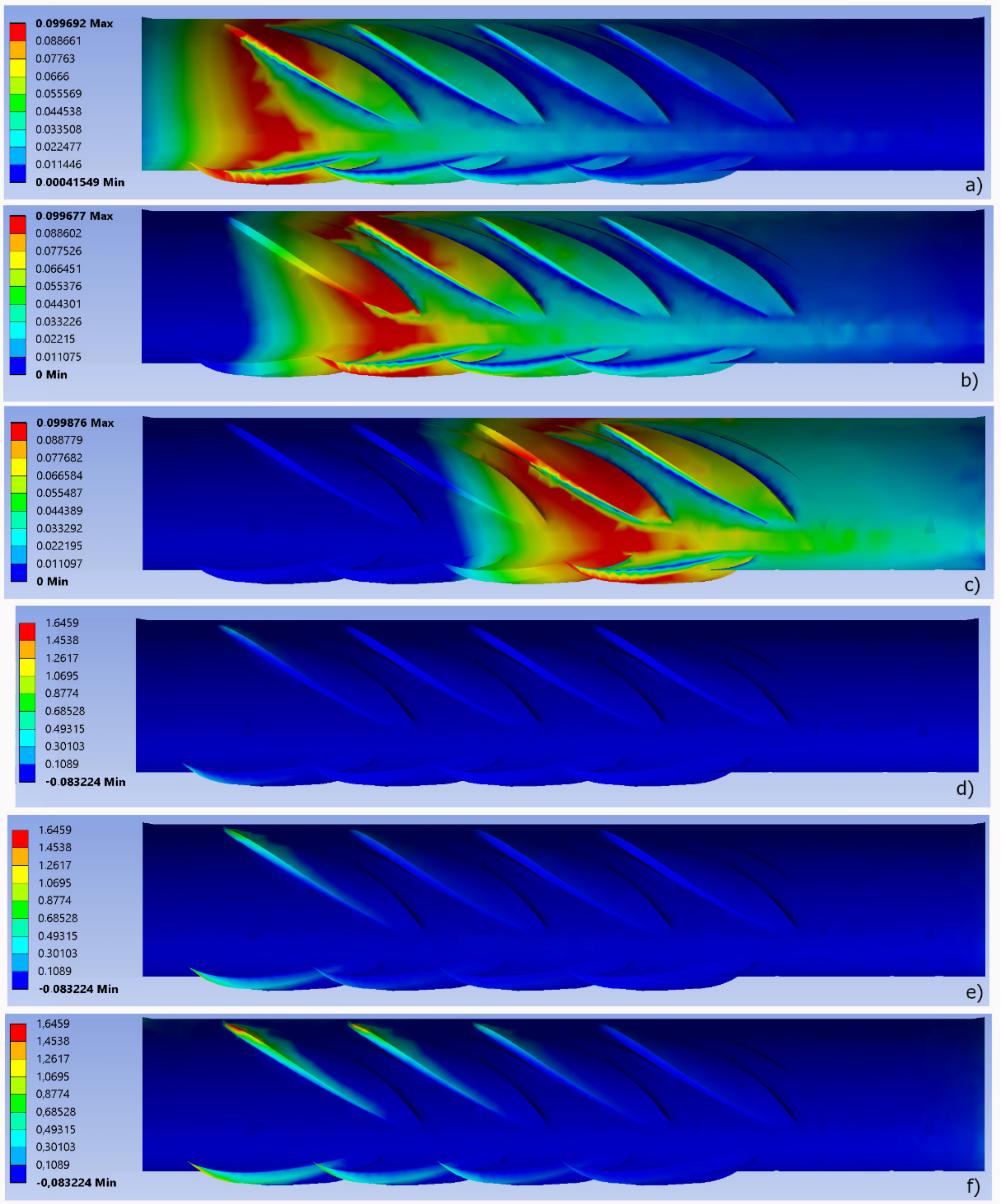

Figure 8. Bonding stresses (MPa) in the interface of a rebar embedded in a prism of mortar with Young's modulus of 5.6 GPa and 7.5 mm of effective covering when the base face (face number 1) was fixed. Bonding shear stress distribution when the force transferred from the rebar to the mortar was (**a**) 40% of that transferred under failure; (**b**) 60% of that transferred under failure; and (**c**) 100% of that transferred under failure. Bonding normal stress distribution when the force transferred from the rebar to the mortar was (**d**) 40% of that transferred under failure; (**e**) 60% of that transferred under failure; and (**f**) 100% of that transferred under failure.

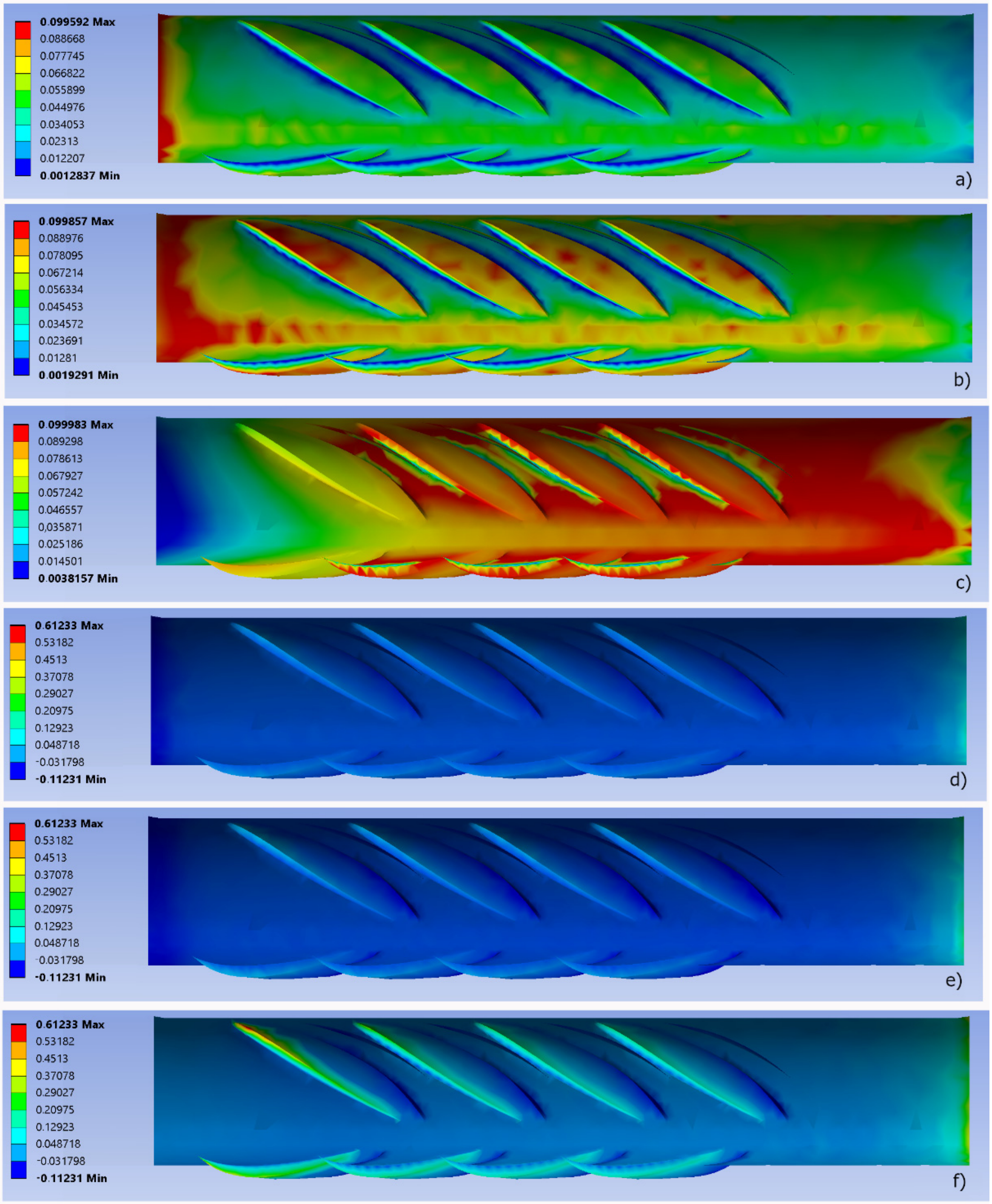

Figure 9. Bonding stresses (MPa) in the interface for a rebar embedded in a prism of mortar with Young's modulus of 5.6 GPa and 7.5 mm of effective covering when three lateral faces (faces number 2, 3, and 4) were fixed. Bonding shear stress distribution when the force transferred from the rebar to the mortar was (**a**) 40% of that transferred under failure; (**b**) 60% of that transferred under failure; and (**c**) 100% of that transferred under failure. Bonding normal stress distribution when the force transferred from the rebar to the mortar was (**d**) 40% of that transferred under failure; (**e**) 60% of that transferred under failure; and (**f**) 100% of that transferred under failure.

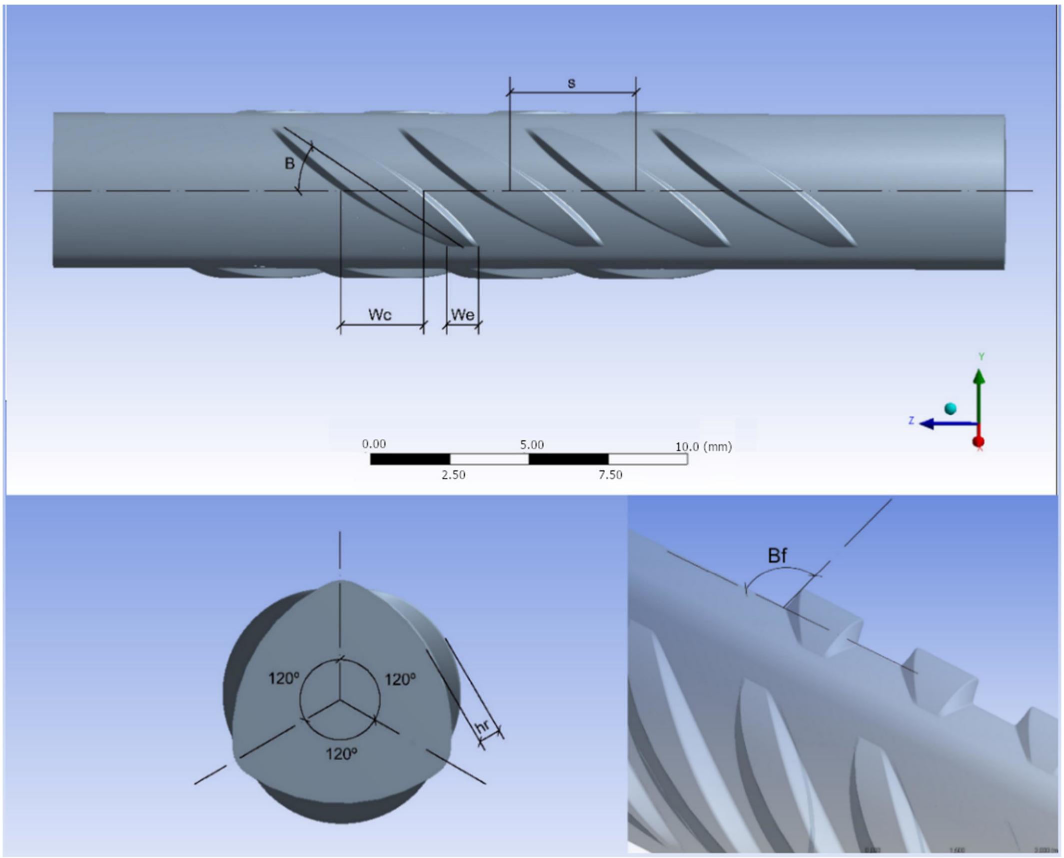

Figure 10. Geometrical parameters of the rebar that ranged in iterative analyses.

In all these analyses, Young's modulus of mortar was set to 5.6 GPa. Boundary conditions of fixation along three and four of the longitudinal faces (faces 3, 4, and 5) of the prism were considered, as well as effective covering for rebars of 6 mm and 25 mm. Results are laid out in Table 2. In order to avoid noise in subsequent calculations, the rebar geometrical parameters were not changed simultaneously.

Table 2. Reaction force *F* (N) needed to displace a 5×10^{-5} mm rebar with different shapes, with effective covering (eff.cov.) 6 mm/ 25 mm and Young´s modulus 5.6 GPa; as boundary conditions, fixation in three or four of the longitudinal faces of the prism.

W_c (mm)	W_e (mm)	B (°)	B_f (°)	h_r (mm)	s (mm)	* F_{3LF}	** F_{4LF}	* F_{3LF}	** F_{4LF}
						eff.cov. = 6 mm		**eff.cov. = 25 mm**	
1	2.5	55	67.5	0.45	4	17.685	20.23	6.494	7.046
1.5						17.77	20.339	6.506	7.059
2						17.861	20.454	6.518	7.074
2.5						17.949	20.567	6.517	7.073
3						18.029	20.66	6.527	7.084
3.5						18.085	20.737	6.536	7.094
2.5	1	55	67.5	0.45	4	17.9	21.122	6.573	7.136
	1.5					17.911	20.72	6.53	7.088
	2					17.935	20.724	6.534	7.092
	2.5					17.949	20.723	6.53	7.088
	3					17.948	20.726	6.532	7.092
	3.5					17.972	20.742	6.532	7.09

Table 2. *Cont.*

W_c (mm)	W_e (mm)	B (°)	B_f (°)	h_r (mm)	s (mm)	* F_{3LF}	** F_{4LF}	* F_{3LF}	** F_{4LF}
						eff.cov. = 6 mm		eff.cov. = 25 mm	
2.5	2.5	15	67.5	0.45	4	18.393	20.756	6.528	7.086
		20				18.071	20.546	6.518	7.073
		25				18.075	20.567	6.517	7.073
		30				18.074	19.958	6.457	7.002
		35				18.078	20.13	6.474	7.022
		40				18.093	20.327	6.494	7.045
		45				18.1	20.567	6.517	7.072
		50				17.934	20.817	6.545	7.105
		55				17.949	21.085	6.574	7.14
2.5	2.5	55	45	0.45	4	17.981	21.363	6.606	7.177
			50			17.907	20.604	6.569	7.132
			55			17.931	20.513	6.519	7.074
			60			17.935	20.544	6.52	7.075
			65			17.95	20.546	6.518	7.074
			70			17.951	20.568	6.519	7.074
			75			17.95	20.567	6.516	7.071
			80			17.943	20.564	6.522	7.078
			85			17.952	20.557	6.526	7.083
			90			17.954	20.567	6.525	7.063
2.5	2.5	55	67.5	0.15	4	17.464	20.571	6.525	7.082
				0.25		17.604	20.503	6.514	7.069
				0.35		17.761	20.517	6.514	7.069
				0.45		17.949	20.548	6.517	7.072
				0.55		18.15	20.567	6.517	7.073
				0.65		18.358	20.563	6.525	7.082
				0.75		18.58	20.597	6.52	7.076
2.5	2.5	55	67.5	0.45	3	18.203	20.888	6.551	7.112
					4	17.949	20.567	6.517	7.073
					5	17.793	20.367	6.503	7.056
					6	17.632	20.166	6.489	7.039

* Reaction force *F* (N) with three fixed longitudinal faces ** Reaction force *F* (N) with four fixed longitudinal faces.

4. Discussion

In this section, the results presented in Section 3 are analyzed and discussed. To better evaluate the influence that the aspects taken into account exert on the final results, several graphical depictions of the results are provided. Thus, Figure 11, which depicts data in Table 1, shows that the Young's modulus of the material that surrounds the rebar clearly influences the final value of *F*.

Regarding the relationships between values of *F*, the improvement rate of this parameter using mortars with Young's modulus of either 5.6 or 10 GPa is almost linear, and this improvement is also independent of boundary conditions and the thickness of effective coverings. That is, while Young's modulus increases by 178.6%, the median of the values of *F* assumes 173.2% with a standard deviation of 0.03. With higher values of the Young´s modulus, the correlation becomes less clear, since it is much more dependent on the effective covering and boundary conditions. When this increases by 297% (that is, it takes a value of 20 GPa), there is almost a linear relationship between this value and *F* only when Face 1 is fixed, since this value assumes 283% with a standard deviation of 0.01, while the respective values for two, three and four fixed lateral faces (Faces 2, 3, 4, and 5) are 331% and 0.40; 315% and 0.84; 304% and 1.48, respectively. This undoubtedly leads to the fact that the results from the pull-out test cannot be extrapolated to the usual situation of rebars in which the boundary conditions are different to those of the test. When Young's modulus of mortars is 50 GPa, this correlation is impossible since the standard deviation reaches inadmissible values. On the other hand, a certain proportionality between values is found in the results for 20 GPa. When effective coverings are either 6 mm or 7.5 mm, no relevant difference can be found between values obtained from prisms with three or four fixed faces. In contrast, when effective coverings are 10, 12.5, 15 or 25 mm, differences of 2.38%, 2.82%, 2.57% and 2.18%, respectively, are found. Regarding global results in terms of Young's modulus and effective coverings, the higher these results, the more homogeneous *F* becomes. Figure 11d depicts this fact clearly, where fixation of Face 1 and 6 mm of effective covering assumes approximate values of *F* less than 50% of those attained with an effective covering of 12.5 mm or higher.

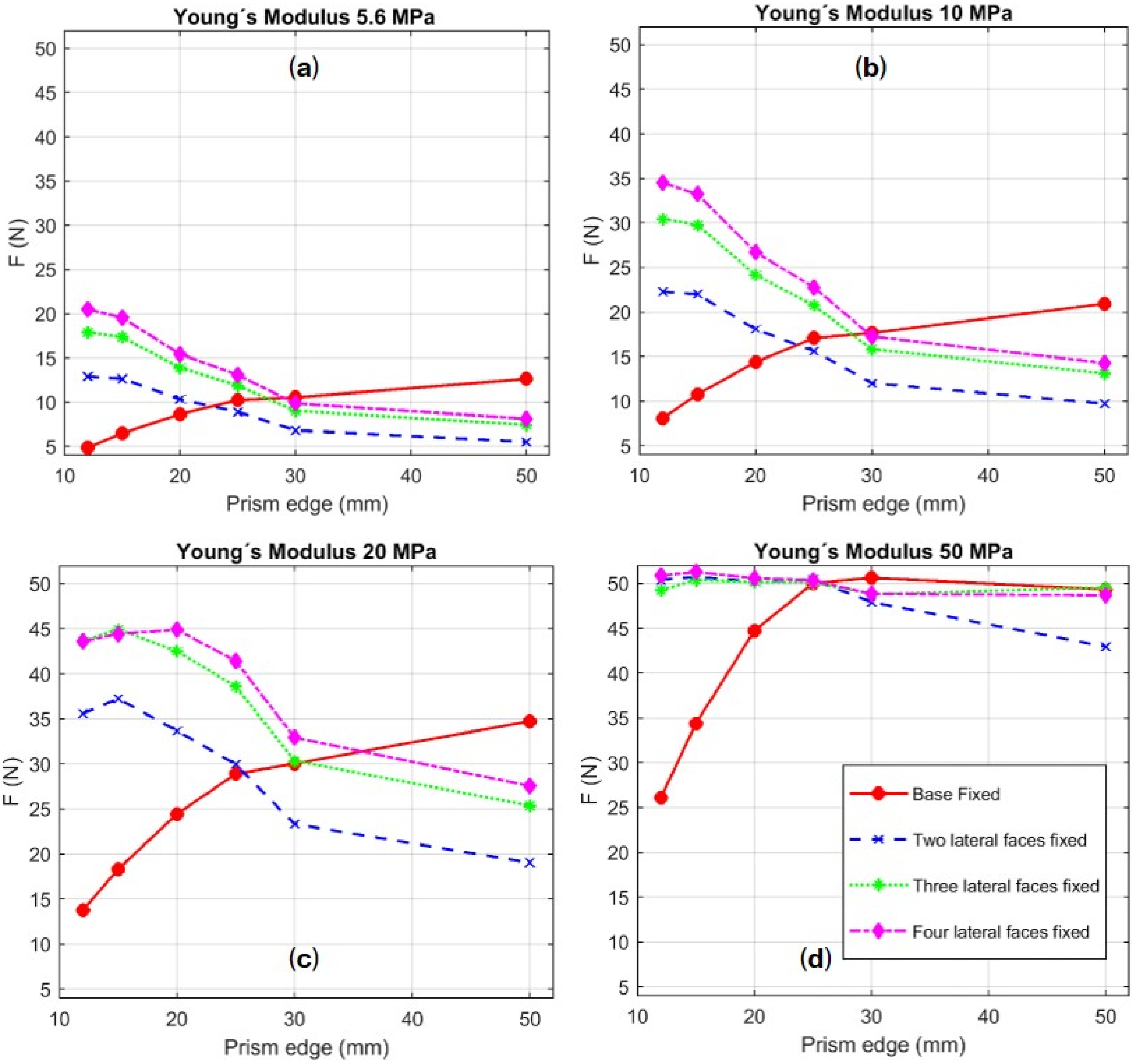

Figure 11. Chart depicting the reaction force *F* (N) produced by a 5×10^{-5} mm displacement of a rebar embedded in mortar prisms with different edges, different Young's modulus and different boundary conditions: (**a**) Mortar with Young's modulus of 5.6 GPa; (**b**) mortar with Young's modulus of 10 GPa; (**c**) mortar with Young's modulus of 20 GPa; (**d**) mortar with Young's modulus of 50 GPa.

Figure 11 also demonstrates that boundary conditions constitute key data for the definition of the value of *F*. It is easy to observe that, while lateral fixations assume a decrease when the effective covering is thicker, fixation in Face 1 produces the opposite effect. This fact has a clear implication in the quantification of bonding by pull-out tests in rebars subjected to these conditions, since the bonding behavior is not correctly reproduced in this test. The number of faces that are fixed also affects the value of F: the more fixed faces there are, the higher F becomes. This fact is linked to the equivalent strain energy (η^{mic}) in the microplane model (Equation (1)).

When only Face 1 is fixed and the rebar is embedded in a 12 × 12 mm^2 section prism, the highest values of equivalent strain energy are concentrated close to the bounded face (Figure 12 right). Ribs transfer load to the medium, but, under these circumstances, the ribs placed in positions that are far from the fixation hardly make any contribution to this transfer. As the effective covering increases, a higher number of ribs contribute to this mechanism and, consequently, the value of F increases (Figure 12 left).

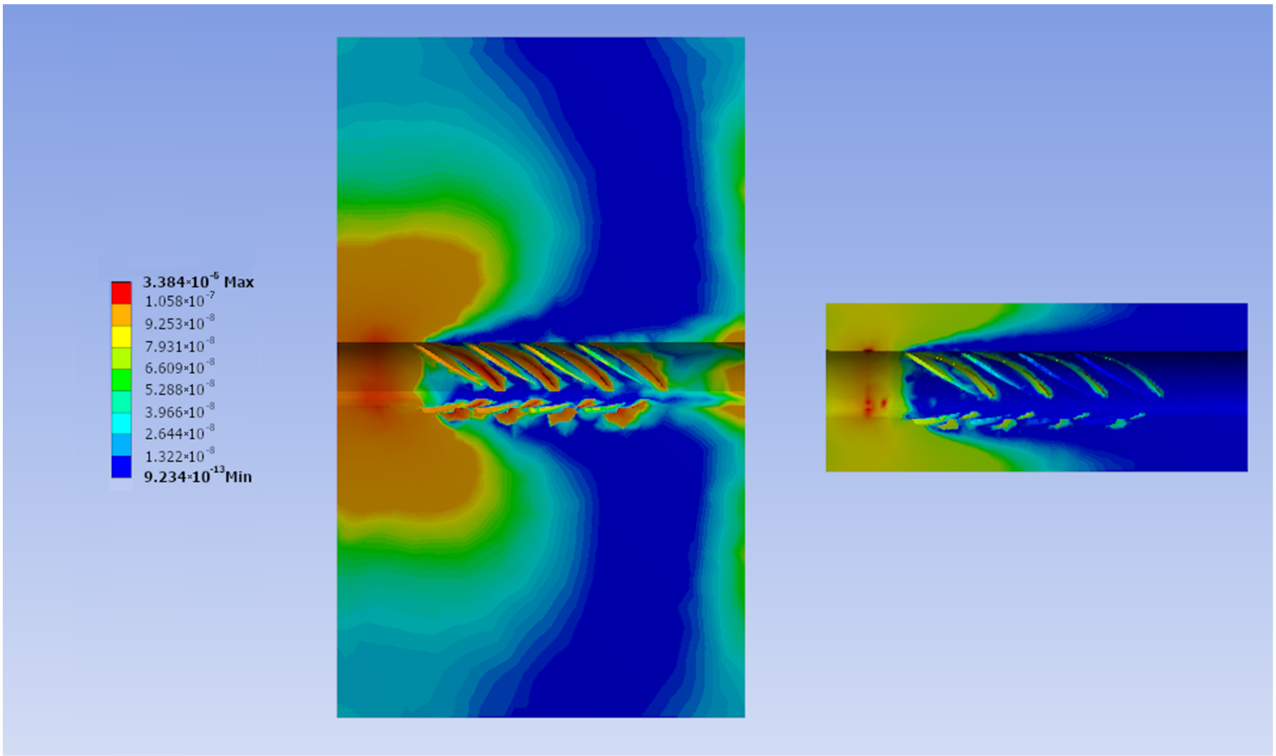

Figure 12. Equivalent strain energy distribution in the mortar joints (E = 5.6 GPa) when face 1 of the prism is fixed and 5×10^{-5} mm displacement is applied to the base of the rebar: (**left**) base section of 50 x 50 mm^2; (**right**) base section of 12 × 12 mm^2.

When lateral faces of the prism are fixed, bonding shear stress decreases while effective covering increases. The value of F, as the integral of the stresses, obviously also decreases. Fixation in lateral faces produces a confinement effect in the bar (especially in the case of reduced coverings) that notably improves its bonding behavior. Since this effect does not exist when only the base face of the prism (Face 1) is fixed, the bonding behavior of rebars is completely different (Figure 13). Bond shear stress is higher in the case of reduced covering (Figure 13a). This justifies the reduction of F observed in Figure 11 when the covering increases in the cases of lateral restraint (Figure 13b).

Regarding the rib shape, the Pearson product moment correlation matrix based on data presented in Table 2 is obtained, thus obtaining the influence for each one of the six geometrical parameters of the rib (*Wc, We, B, Bf, hr, s*). This matrix is non-dependent on the number of faces that are fixed. In contrast, it is strongly dependent on the thickness of the effective covering (Table 3).

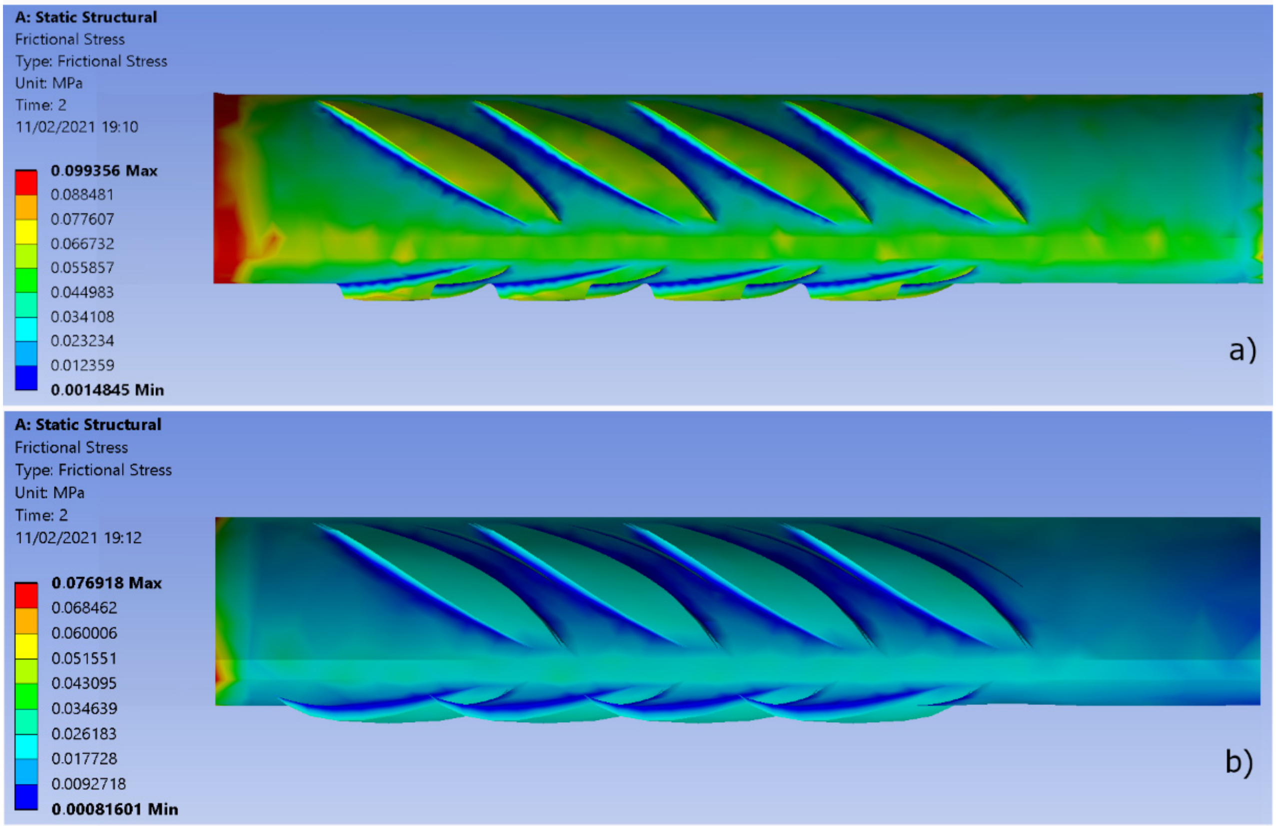

Figure 13. Distribution of bond shear stress (MPa) in the interface in a prism of mortar (E = 5.6 MPa) for a displacement equal to 5 × 10^{-5} mm when Faces 2, 3, and 4 are fixed, for a prism with dimensions: (**a**) 12 × 12 mm^2; (**b**) 50 × 50 mm^2.

Table 3. Pearson correlation coefficient of each geometrical parameter of the rib in bonding behavior.

Effective Covering	W_c	W_e	B	B_f	h_r	s
6 mm	0.30	0.06	0.38	0.01	0.78	−0.35
25 mm	0.22	0.07	0.28	−0.11	0.80	−0.29

The most influential geometrical parameter is, undoubtedly, h_r, while both B and s exert only a medium influence. Rib height in the center (h_r) has also medium influence in bonding, but this influence is reduced to 27% as the effective covering increases. The effect of B_f and W_e in bonding is irrelevant. Regarding s, although it is demonstrated that high values of this parameter positively influence bonding [45,54], a negative value in the coefficient (Table 3) implies the opposite. Spacing between ribs is also linked to the number of ribs that fit into a fixed length of bar: the greater the rib spacing, the fewer ribs in the 30-mm-length bar. In this research, the lowest number of ribs that involves high rib spacing, and the subsequent negative influence on bonding, carry more weight than the positive effect of higher values of this parameter.

A regression analysis with the values obtained in this research (Table 2) reveals the relationship between the geometrical parameter of the ribs and the value of F for the case of the rebar embedded in the prism with three and four lateral faces (F_{3LF}- F_{4LF}) fixed in prisms of 12 × 12 and 50 × 50 mm^2.

$$F_{3LF(12X12)} = 17.0659 + 0.1693W_c + 0.0316W_e + 0.0067B + 0.0002B_f + 1.8732h_r - 0.176s \tag{7}$$

$$F_{4LF(12X12)} = 19.4548 + 0.2138W_c + 0.0405W_e + 0.0083B + 0.0002B_f + 2.3625h_r - 0.2224s \tag{8}$$

$$F_{3LF(50X50)} = 6.4397 + 0.0162W_c + 0.0048W_e + 0.0067B + 0.0004B_f + 0.2493h_r - 0.0191s \tag{9}$$

$$F_{4LF(50X50)} = 6.9887 + 0.0186W_c + 0.0054W_e + 0.0007B + 0.0006B_f + 0.2932h_r - 0.0224s \tag{10}$$

Equations (7)–(10) are highly reliable since (i) R-square coefficients are 94.64%, 94.64%, 86.83%, and 87.50%; (ii) the residual standard deviations are 0.0497, 0.0627, 0.0101, and 0.0115; (iii) the mean absolute errors (MAEs) are 0.0298, 0.0377, 0.0064, and 0.0073, and (iv) the Durbin Watson (DB) statistic is 2.1857, 2.1717, 1.9809, and 2.1285. These equations, together with Figure 10, allow us to relate the results from this research to different shapes of ribs.

5. Conclusions

This paper deals with the bonding behavior of rebars under the special circumstances that occur when masonry is reinforced. Thicknesses of coverings that are lower than usual, together with variable boundary conditions, involve different behavior of rebars in terms of bonding.

This research covers the cases of stainless steel rebars with 5 mm diameter, embedded in mortar joints with Young's modulus of 5.6, 10, 20, and 50 GPa, and effective coverings of 6, 7.5, 10, 12.5, 15, and 25 mm. Furthermore, the variability of the boundary conditions is taken into account by the fixation of two, three or four longitudinal faces of the prisms into which the bars are embedded, as well as their bases. In this way, several of the most frequent performances of this reinforcement are reproduced: bed joint structural repointing, transversal anchors in walls, meshes attached to wall surfaces, and the conditions of the standard pull-out test. By changing Young's modulus, the use of standard poor mortars to high-strength binders is encompassed.

A pull-out test with no embracement of the samples does not reproduce the behavior of the bars under these conditions. When the prisms that surround the rebars are not embraced, maximum reaction force increases with effective covering, decreasing in the opposite case.

Regarding values of this, when the Young's modulus of the mortar reaches 10 GPa, the relationship between both parameters is linear. In this way, the results can be extrapolated for various materials. This fact only occurs in high-performance mortars when only the base of the prism is fixed. These facts lead to the conclusion that rebars must be tested under the boundary conditions in which they will work.

Regarding the shape of the rebars, the most influential geometrical aspects of the ribs are identified. Although rib height is obviously the key value in bonding, the contribution of the other aspects, such as central width, angle between rib and rebar axes, and rib spacing, depends on boundary conditions and effective coverings. The rib central width is of major importance when effective covering is low and the bar is highly confined, but this importance decreases when effective covering increases. For a fixed length of bar, as used in this research, the spacing between ribs has a negative influence on bonding. As a result, several relationships between the rebar shape and the results obtained in terms of bonding are attained.

Author Contributions: Conceptualization, F.A., E.R.-M. and B.H.; investigation, F.A. and E.R.-M.; Methodology, F.A., E.R.-M. and B.H.; project administration, E.R.-M. and B.H.; resources, F.A.; supervision, B.H.; writing–original draft, E.R.-M.; writing–review & editing, F.A. and B.H. All authors have read and agreed to the published version of the manuscript.

Funding: This research has been carried out under the project PGC2018-098185-A-I100, funded by: FEDER/Ministerio de Ciencia e Innovación-Agencia Estatal de Investigación of Spain.

Institutional Review Board Statement: Not applicable.

Informed Consent Statement: Not applicable.

Acknowledgments: The authors wish to thank the undergraduate students David Perejon and Marcos García for their contribution.

Conflicts of Interest: The authors declare no conflict of interest.

Appendix A

Table summarizing the values of reaction force F (N) needed to pull a 5-mm rebar out a distance of 5×10^{-5} mm from its initial position embedded in a 100-mm edge cube of mortar, when different combinations of bond shear stress and bond tensile stress in the CZM are set and the frontal face of the cube is fixed.

Maximum Bond Shear Stress (MPa)	**Maximum Bond Tensile Stress (MPa)**	**Reaction Force F (N)**
0.10	0.10	14.333
	0.25	14.346
	0.50	14.348
	1.00	14.349
0.25	0.10	17.825
	0.25	17.859
	0.50	17.864
	1.00	17.866
0.50	0.10	21.362
	0.25	21.432
	0.50	21.444
	1.00	21.446
1.00	0.10	26.654
	0.25	27.003
	0.50	27.074
	1.00	27.092

References

1. Candela, M.; Borri, A.; Corradi, M.; Righetti, L. Effect of transversal steel connectors on the behavior of rubble stone-masonry walls: Two case studies in Italy. In Proceedings of the Brick Block Mason. Trends, Innov. Challenges—Proc. International Brick and Block Masonry Conference IBMAC 2016, Padova, Italy, 26–30 June 2016; pp. 2029–2038. [CrossRef]
2. Corradi, M.; Castori, G.; Borri, A. Repairing brickwork panels using titanium rods embedded in the mortar joints. *Eng. Struct.* **2020**, *221*, 111099. [CrossRef]
3. Valluzzi, M.R.; Binda, L.; Modena, C. Mechanical behaviour of historic masonry structures strengthened by bed joints structural repointing. *Constr. Build. Mater.* **2005**, *19*, 63–73. [CrossRef]
4. Binda, L.; Modena, C.; Saisi, A.; Tongini-Folli, R.; Valluzzi, M.R. Bedjoint structural repointing of historic masonry structures. In *Proceedings of the 9th Canadian Masonry Symposium, Fredericton, NB, Canada, 4–6 June 2001*; Bischoff, P.H., Dawe, J.L.D., Eds.; Department of Civil Engineering, University of New Brunswick: Frederickton, NB, Canada, 2001.
5. Anzani, A.; Cardani, G.; Condoleo, P.; Garavaglia, E.; Saisi, A.; Tedeschi, C.; Tiraboschi, C.; Valluzzi, M.R. Understanding of historical masonry for conservation approaches: The contribution of Prof. Luigia Binda to research advancement. *Mater. Struct. Constr.* **2018**, *51*, 1–27. [CrossRef]
6. Valluzzi, M.R. On the vulnerability of historical masonry structures: Analysis and mitigation. *Mater. Struct. Constr.* **2007**, *40*, 723–743. [CrossRef]
7. Corradi, M.; Di Schino, A.; Borri, A.; Rufini, R. A review of the use of stainless steel for masonry repair and reinforcement. *Constr. Build. Mater.* **2018**, *181*, 335–346. [CrossRef]
8. Meriggi, P.; de Felice, G.; De Santis, S. Design of the out-of-plane strengthening of masonry walls with fabric reinforced cementitious matrix composites. *Constr. Build. Mater.* **2020**, *240*, 122452. [CrossRef]

9. Ascione, L.; Carozzi, F.G.; D'Antino, T.; Poggi, C. New Italian guidelines for design of externally bonded Fabric-Reinforced Cementitious Matrix (FRCM) systems for repair and strengthening of masonry and concrete structures. *Procedia Struct. Integr.* **2018**, *11*, 202–209. [CrossRef]
10. Ceroni, F.; Darban, H.; Luciano, R. Analysis of bond behavior of injected anchors in masonry elements by means of Finite Element Modeling. *Compos. Struct.* **2020**, *241*, 112099. [CrossRef]
11. Gentilini, C.; Finelli, F.; Girelli, V.A.; Franzoni, E. Pull-out behavior of twisted steel connectors employed in masonry: The influence of the substrate. *Constr. Build. Mater.* **2021**, *274*, 122115. [CrossRef]
12. Mayorga, E.R.; Ancio, F.; Hortigon, B. Optimisation of stainless steel rebars to repair masonry structures. In Proceedings of the REHABEND Construction Pathology, Rehabilitation Technology and Heritage Management, Granada, Spain, 28–30 September 2020.
13. Siderurgia, A. 36 UNE 36740: Adherence Test for Steel for Reinforcement of Concrete. Beam Test. *UNE*. 1998. Available online: https://www.techstreet.com/ashrae/standards/une-36740-1998?product_id=1300670 (accessed on 10 May 2021).
14. BS EN 1881:2006. *Products and Systems for the Protection and Repair of Concrete Structures—Test Methods—Testing of Anchoring Products by Pull-Out Method*; British Standard Institute: London, UK, 2006; ISBN 0580 49827 1.
15. BS EN 846-2:2000. *Methods of Test for Ancillary Components for Masonry—Part 2: Determination of Bond Strength of Prefabricated Bed Joint Reinforcement in Mortar Joints*; British Standard Institute: London, UK, 2000; ISBN 0580 34889 X.
16. RILEM (Ed.) RILEM-TC RC 6 Bond test for reinforcement steel. 2. Pull-out test, 1983. In *RILEM Recommendations for the Testing and Use of Constructions Materials*; E & FN SPON: New York, NY, USA, 1994; pp. 218–220. ISBN 2351580117.
17. ACI Committee 440 Guide Test Methods for Fiber-Reinforced Polymers (FRPs) for Reinforcing or Strengthening Concrete Structures, ACI 440.3R-12. 2012. Available online: https://www.concrete.org/store/productdetail.aspx?ItemID=440312&Language=English&Units=US_AND_METRIC (accessed on 10 May 2021).
18. Chu, S.H.; Kwan, A.K.H. A new method for pull out test of reinforcing bars in plain and fibre reinforced concrete. *Eng. Struct.* **2018**, *164*, 82–91. [CrossRef]
19. Ceroni, F.; Di Ludovico, M. Traditional and innovative systems for injected anchors in masonry elements: Experimental behavior and theoretical formulations. *Constr. Build. Mater.* **2020**, *254*, 119178. [CrossRef]
20. Paganoni, S.; D'Ayala, D. Testing and design procedure for corner connections of masonry heritage buildings strengthened by metallic grouted anchors. *Eng. Struct.* **2014**, *70*, 278–293. [CrossRef]
21. Miranda, M.P.; Morsch, I.B.; Brisotto, D.D.S.; Bittencourt, E.; Carvalho, E.P. Steel-concrete bond behavior: An experimental and numerical study. *Constr. Build. Mater.* **2021**, *271*, 121918. [CrossRef]
22. Ceroni, F.; Darban, H.; Caterino, N.; Luciano, R. Efficiency of injected anchors in masonry elements: Evaluation of pull-out strength. *Constr. Build. Mater.* **2021**, *267*, 121707. [CrossRef]
23. Hu, X.; Peng, G.; Niu, D.; Wu, X.; Zhang, L. Bond behavior between deformed steel bars and cementitious grout. *Constr. Build. Mater.* **2020**, *262*, 120810. [CrossRef]
24. ANSYSInc Element Library. *Ansys® Academic Research Mechanical, Release 20.2 Help System*; ANSYS Inc.: Canonsburg, PA, USA, 2020.
25. Hortigón, B.; Ancio, F.; Rodriguez-Mayorga, E. Parameterization of stainless steel rebars to improve bonding strength in masonry repairing. In Proceedings of the PROHITECH 2020 4th International Conference on Protection of Historical Constructions, Athens, Greece, 25–27 October 2021.
26. Taylor, G.I. Plastic strain in metals. *J. Inst. Met.* **1938**, *62*, 307–324.
27. Batdorf, S.B.; Budiansky, B. *A Mathematical Theory of Plasticity Based on the Concept of Slip*; National Advisory Committee for Aeronautics, Ed.; NACA Technology: Langley, VA, USA, 1949.
28. Bažant, Z.P.; Prat, P.C. Microplane model for brittle-plastic material: I. Theory. *J. Eng. Mech.* **1988**, *114*, 1672–1688. [CrossRef]
29. Bažant, Z.P.; Prat, P.C. Microplane model for brittle-plastic material: II. verification. *J. Eng. Mech.* **1988**, *114*, 1689–1702. [CrossRef]
30. Bazant, Z.P.; Gambarova, P.G. Crack Shear in Concrete: Crack Band Microplane Model. *J. Struct. Eng.* **1984**, *110*, 2015–2036. [CrossRef]
31. Carol, I.; Bažant, Z.P. Damage and plasticity in microplane theory. *Int. J. Solids Struct.* **1997**, *34*, 3807–3835. [CrossRef]
32. Bazant, Z.P.; Adley, M.D.; Carol, I.; Jirásek, M.; Akers, S.A.; Rohani, B.; Cargile, J.D.; Caner, F.C. Large-strain generalization of microplane model for concrete and application. *J. Eng. Mech.* **2000**, *126*, 971–980. [CrossRef]
33. Caner, F.C.; Bazant, Z.P. Microplane model M4 for concrete. II: Algorithm and calibration. *J. Eng. Mech.* **2000**, *126*, 954–961. [CrossRef]
34. de Vree, J.H.P.; Brekelmans, W.A.M.; van Gils, M.A.J. Comparison of nonlocal approaches in continuum damage mechanics. *Comput. Struct.* **1995**, *55*, 581–588. [CrossRef]
35. Mazars, J.; Pyaudier-Cabot, G. Continuum damage theory—Application to concrete. *J. Eng. Mech.* **1989**, *115*, 345–365. [CrossRef]
36. Peerlings, R.H.J.; de Borst, R.; Brekelmans, W.A.M.; Geers, M.G.D. Gradient-enhanced damage modelling of concrete fracture. *Mech. Cohesive-Frictional Mater.* **1998**, *3*, 323–342. [CrossRef]
37. Geers, M.G.D.; De Borst, R.; Brekelmans, W.A.M.; Peerlings, R.H.J. Strain-based transient-gradient damage model for failure analyses. *Comput. Methods Appl. Mech. Eng.* **1998**, *160*, 133–153. [CrossRef]
38. Zreid, I.; Kaliske, M. A gradient enhanced plasticity–damage microplane model for concrete. *Comput. Mech.* **2018**, *62*, 1239–1257. [CrossRef]

39. Binda, L.; Fontana, A.; Frigerio, G. *Mechanical Behaviour of Brick Masonries Derived from Unit and Mortar Characteristics. Proceedings of the 8th International Brick and Block Masonry Conference IB2MAC, Dublin, Ireland, 19–21 September 1988*; Courcy, J.W.T., Ed.; Elsevier Applied Science: Amsterdam, The Netherlands; Dublin, Ireland, 1988; pp. 205–216.
40. Kaklis, K.N.; Maurigiannakis, S.P.; Agioutantis, Z.G.; Maravelaki-Kalaitzaki, P. Characterization of pozzolanic lime mortars used as filling material in shaped grooves for restoring member connections in ancient monuments. *Int. J. Archit. Herit.* **2018**, *12*, 75–90. [CrossRef]
41. Baltazar, L.G.; Henriques, F.M.A.; Cidade, M.T. Grouts with improved durability for masonry consolidation: An experimental study with non-standard specimens. In *Key Engineering Materials*; Trans Tech Publications Ltd.: Bach, Switzerland, 2017; Volume 747.
42. Luso, E.; Lourenço, P.B. Experimental laboratory design of lime based grouts for masonry consolidation. *Int. J. Archit. Herit.* **2017**, *11*, 1143–1152. [CrossRef]
43. Arandigoyen, M.; Alvarez, J.I. Pore structure and mechanical properties of cement-lime mortars. *Cem. Concr. Res.* **2007**, *37*, 767–775. [CrossRef]
44. Thamboo, J.; Dhanasekar, M. Assessment of the characteristics of lime mortar bonded brickwork wallettes under monotonic and cyclic compression. *Constr. Build. Mater.* **2020**, *261*, 120003. [CrossRef]
45. Tao, W.; Chen, C.; Jun, H.; Ting, R. Effect of bolt rib spacing on load transfer mechanism. *Int. J. Min. Sci. Technol.* **2017**, *27*, 431–434. [CrossRef]
46. Barbosa, M.T.; Sánchez Filho, E.d.S.; de Oliveira, T.M.; Santos, W.J. dos Analysis of the relative rib area of reinforcing bars pull out tests. *Mater. Res.* **2008**, *11*, 453–457. [CrossRef]
47. Chiriatti, L.; Mercado-Mendoza, H.; Apedo, K.L.; Fond, C.; Feugeas, F. A study of bond between steel rebar and concrete under a friction-based approach. *Cem. Concr. Res.* **2019**, *120*, 132–141. [CrossRef]
48. Araújo, A.S.; Oliveira, D.V.; Lourenço, P.B. Numerical study on the performance of improved masonry-to-timber connections in traditional masonry buildings. *Eng. Struct.* **2014**, *80*, 501–513. [CrossRef]
49. Kabir, R.; Islam, M. Bond stress behavior between concrete and steel rebar: Critical investigation of pull-out test via Finite Element Modeling. *Int. J. Civ. Struct. Eng.* **2014**, *5*, 80–90. [CrossRef]
50. Zhao, W.; Zhu, B. Basic parameters test and 3D modeling of bond between high-strength concrete and ribbed steel bar after elevated temperatures. *Struct. Concr.* **2017**, *18*, 653–667. [CrossRef]
51. Allen, J.H.; Felder, A.L.; McDermott, J.F.; Frosch, R.J.; Mitchell, D.; Eligehausen, R.; Leon, R.T.; Pantazopoulou, S.J.; Azizinamini, A.; Fagundo, F.E.; et al. ACI Committee 408 Bond and Development of Straight Reinforcing Bars in Tension Reported by ACI Committee 408. *ACI* **2003**, *408–03*, 1–49.
52. International Organization for Standardization. *Standardization, I.O. for ISO 6935-2:2019 Preview Steel for the Reinforcement of Concrete. Part 2: Ribbed Bars*; ISO: Geneva, Switzerland, 2019.
53. Astm. *A 615/A 615M—09B Standard Specification for Deformed and Plain Carbon-Steel Bars for Concrete Reinforcement*; Astm: West Conshohocken, PA, USA, 2012. [CrossRef]
54. Lorrain, M.S.; Caetano, L.F.; Silva, B.V.; Gomes, L.E.S.; Barbosa, M.P.; Silva Filho, L.C.P. Bond strength and rib geometry: A comparative study of the influence of deformation patterns on anchorage bond strength. In Proceedings of the PCI Annual Convention & 3rd International FIB Congress FIB, Washington, DC, USA, 29 May–2 June 2010.